On dissipated energy density in compression for concrete

(Article begins on next page)

16 July 2022

# On dissipated energy density in compression for concrete

Giuseppe FERRO $^\star$

*Politecnico di Torino, Department of Structural Engineering and Geotechnics, Corso Duca degli Abruzzi 24, 10129 Torino, Italy.*

**Abstract** An experimental investigation on drilled cylindrical concrete specimens in compression over a large scale range (1:19) has been carried out to evaluate the variation of some mechanical parameters by varying specimen size. The peculiarity of the present investigation consists in exploring very small specimen dimensions. The experimental results show scale effects on dissipated energy density rather than on uniaxial compressive strength. A theoretical explanation for such a phenomenon, based on fractal hypothesis, is presented and a comparison between experimental and theoretical values is discussed.

**Keywords**: Fracture mechanisms, powder compaction, concrete, structures, mechanical testing.

$^\star$  Address: Politecnico di Torino, Department of Structural Engineering and Geotechnics,
Corso Duca degli Abruzzi 24, 10129 Torino, Italy.
Tel. +39.11.5644885, Fax. +39.11.5644899, e-mail:ferro@polito.it

**NOMENCLATURE**

$\delta$ = displacements;

$\epsilon$ = strain;

$\epsilon_{peak}$ = strain at the peak stress;

$d$= specimen diameter ;

$h$= specimen height chosen as the characteristic specimen size;

$\epsilon_m$= mean deformation;

$f'_c$= compression strength;

C1= smallest specimen set with $h$=10 mm;

C2= specimen set with $h$=23 mm;

C3= specimen set with $h$=46 mm;

C4= specimen set with $h$=100 mm;

C5= largest specimen set with $h$=190 mm;

C33= third specimen of the set with $h$=46 mm;

$N$= number of fragments in fragmentation process;

$r$= characteristic linear dimension of fragments;

$B$= constant of proportionality;

$D$= fractal dimension of the fragmentation process;

$V_f$= total volume (mass) of fragments;

$r_{max}$= characteristic linear dimension of the largest fragment;

$r_{min}$= characteristic linear dimension of the smallest fragment;

$k$= constant of proportionality;

$V$= volume of the un-fragmented specimen;

$A_f$= total surface area of the fragments;

$C$= geometrical factor depending upon the average shape of the fragments;

$W$= energy dissipated to produce a new free surface in the fragmentation process;

$\beta_F$= specific energy absorbing capacity;

$\mathcal{G}$= elastic energy release rate or specific energy necessary to generate the unit area of fracture;

$d_\omega$= fractal dimension of the fragmented set=3-D;

$h^*$= measure of the fractal set representing the fragmented configuration;

$S$= dissipated energy density;

$\mathcal{G}_F^*$=fractal dissipated energy density parameter;

$\epsilon^*$= renormalized fractal strain;

$E^*$= renormalized fractal elastic modulus;

# 1  INTRODUCTION

The advent of computers has considerably changed the capabilities in design and analysis of concrete structures. The extensive use of powerful computers and finite elements codes in structural analysis is meaningful only if suitable and reliable constitutive laws for the material are available. In design, however, concrete is generally classified on the basis of its compressive strength. A correct evaluation is therefore

fundamental.

In general, the constitutive relations and the mechanical parameters for concrete are obtained from standard specimens. The sizes and shapes of compressive strength test specimens of concrete vary from one country to another. Commonly used standard sizes are 150 mm for cubes and $150 \times 300$ mm for cylinders. The introduction of high-strength concrete, with compression strength up to five times the standard strength, suggests the use of smaller specimens, with the advantages of maintaining the standard test machines available in the laboratories, easy handling, and using less concrete. Another important application of reducing specimen sizes is constituted by the determination of the concrete strength for existing structures by drilling small specimens. This technique is very useful, the deterioration of the mechanical properties for concrete structures being one of the main problems in Civil Engineering.

The choice of the standard size is affected by the variation of the compressive strength with size and height/diameter (or slenderness) ratio. This variation is high when the rigid test machine platens are in direct contact with the concrete specimen,the lateral deformation of concrete being restrained at the specimen ends. A wide investigation has been carried out by Carpinteri et al. [1].

Very interesting results have been obtained in a round robin test organized by the RILEM Committee 148 SSC "Strain-Softening of Concrete" [2], whose aim was to investigate the softening behavior of concrete by varying specimen dimensions, boundary conditions, feed-back signals and testing machine characteristics. They observed the independence of the slenderness (or size) on the compressive strength, when the boundary conditions of the concrete specimens were characterized by no friction (or reduced friction) at the ends.

The effect of size on the mechanical properties of concrete is also important when small scale models are used to predict the behavior of real structures. Early work on the size effect in compression dates back to the 1920's. Gonnermann [3] emphasized the size effects through an extensive investigation on the compressive strength of cylinders with a height/diameter ratio equal to two.

Many other authors fronted the problem of size effects on nominal strength for concrete in compression. Blanks and McNamara [4] performed tests on cylindrical specimens with slenderness of $h/d=2$ in a large scale range (1:12), while Jishan and Xixi [5] performed experiments on cubes (scale range 1:4) and on prisms with $h/d=3$ (scale range 1:3). Other analyses on size effects in compression were conducted by considering particular geometries, as compact compression tests [6] , reinforced concrete columns [7] and high-strength concrete reinforced with randomly distributed fibers [8]. Several assessments were made on the size effects through the extensive experimental work reported in the literature [9].

The nominal compressive strength is obtained by dividing the peak force by the initial specimen cross-section area. This operation has the meaning of estimating a global material property, ignoring at the same time the material structure as

3

well as the material failure behavior during the test. Momber [10] analyzed the fragmentation of standard concrete cylinders under compression. He observed that the standard codes (ASTM C39-86) consider types of failure which involve only large primary fracture debris, while after compression testing of any concrete specimen, fragments of fine-grained material are generated. Slate and Hover [11] showed pervasive internal crack growth up to the peak load by studying the interior of concrete specimens that were loaded up to a certain level and that were subsequently unloaded. From their experimental observations, it is believed that energy dissipation in the pre-peak regime is a global continuum-dominated process that may be attributed to microcracking throughout the entire specimen. On the other hand, energy dissipation in the post-peak regime is a localized surface-dominated fracture process after the coalescence of microcracks in the peak regime. Vardoulakis et. al. [12] proposed a continuum fracture mechanics of uniaxial compression on brittle materials to arrive at a continuum description of the observed post-peak phenomena. Their conclusions, based on experimental evidence and dimensional analysis, state that the post-peak axial stress is a function of the axial displacement normalized by the radius of the specimen, and not by its height. Van Vliet and van Mier [13], observed that post-peak data from uniaxial compression experiments on plain concrete suggest a stress-displacement rather than a stress-strain relation.

An extensive experimental investigation on geometrically similar cylindrical concrete specimens in compression obtained by a unique concrete block is herein presented to evaluate the variation of some mechanical parameters by varying specimen size on a very large scale range (1:19) and by avoiding frictional restraint between the loading platens and the specimen. The pecularity of the present investigation consists in exploring very small specimen dimensions. One of the main goals of the present paper is the measure of the energy dissipated in destroying or fragmenting a volume of concrete.

From a phenomenological point of view, the softening branch of the load-displacement curve is governed by macrocracking, after the coalescence of the initial microcracks. As shown by the experimental results, the ultimate compressive strength of concrete depends on the type of testing machine, the specimen size and the nature of the contact between the machine platens and the specimen. In this paper, it is shown how, avoiding friction, the strength is almost independent of specimen dimension, whereas strong variations are observed for dissipated energy density in compression. A theoretical explanation, recently proposed by Carpinteri and Pugno [14,15], for the scale effects on the dissipated energy density in compression is discussed and applied to the experimental results. This is based on the concept of fractal geometry [16,17], and on the fragmentation approach [18]. From the theory, it can be shown how, in the scale range of the tested specimens, the energy dissipation is a surface-dominated phenomenon and damage localization occurs in small concentrated zones. This statement is valid only for small specimen sizes, while for larger structural dimensions the energy dissipation should be a volume-dominated process and damage is more spatially distributed.

4

## 2  EXPERIMENTAL SETUP

The ambition of testing concrete specimens in compression in a very wide size range strongly impacts with the laboratory set-ups, which opposes physical limits. The fundamental idea was to use a very simple standard testing apparatus composed only of a closed-loop servo-hydraulic system and strain gauges glued on the specimen to record the longitudinal as well as the transverse deformation in the pre-peak part of the force versus displacement curve. As the specimens were very different in size, two different set-ups have been adopted, even if this could cause some inconveniences due to different stiffnesses of the frames.

### 2.1  Test specimens

The first problem was that of defining the size and the slenderness of the test specimens. The size is limited by the dimension of the aggregates (lower limit) and by the potentialities of the available equipment (upper limit).

All the cylinders were obtained by drilling from a unique concrete block with sizes $800 \times 500 \times 200$ mm. The microconcrete used for the specimens is characterized by a maximum aggregate size of 4 mm. The porosity is equal to 17.7 vol % and the distribution of pores is 15.8 % > 10000 nm, 52.9 % 30-10000 nm and 31.3 % < 30 nm. The nominal strength is 51.8 N/mm$^2$ while the compression strength $f'_c$, obtained from cubes ($150 \times 150 \times 150$ mm) after 28 days, is equal to 33 N/mm$^2$. The water-cement ratio is equal to 0.65.

Five different diameters were considered in relation to the disposable drilling core-bits in a scale range of 1:19. The specimens were cylinders with a height/diameter ratio $h/d = 1$ and $h$ chosen as the characteristic dimension equal to 10, 23, 45, 100, 190 mm, respectively. Four specimens have been tested at each size. Two extra specimens for $h = 10$, 23 and 45 mm were used to check the electrical parameters (impedance, gain). The geometries of the tested specimens are presented in Fig. 1.a, while an overview of all the specimen sizes is reported in Fig. 1.b. The geometrical characteristics are reported in Tab.1.

### 2.2  Testing equipment

For the three smallest sizes, the tests were carried out on a uniaxial compression machine with a capacity of 100 kN. The machine is controlled by a closed-loop servo-hydraulic system. Of the two loading platens, the lower is fixed, while the upper is connected to the machine hinge. In this way, the upper platen can adjust to the geometrical imperfections of the specimen. All compression tests with this machine have been performed under displacement control, by imposing a constant rate of the displacement of the upper loading platen. The displacement rate has been set in

order to impose the same stress rate for all the specimen sizes. A stress rate equal to 0.5 N/mm$^2$/s was adopted, as prescribed by UNI Standard 6130 for cubic strength evaluation. To obtain this stress rate, the displacement rates have been set equal to $2 \times 10^{-3}$ mm/s for the smallest specimens ($h$=10 mm, C1), $4.6 \times 10^{-3}$ mm/s for the specimens with $h$=23 mm (C2) and $10 \times 10^{-2}$ mm/s for $h$=46 mm (C3). On each specimen two bidirectional strain gauges were glued, the length of which was taken proportional to the specimen height. More specifically, the strain gauge length was 1.5 mm for $h$=10 mm (strain gauge HBM 1.5/120 xy 11), 3 mm for $h$=23 mm (strain gauge HBM 3/120 xy 11) and 6 mm for $h$=45 mm (strain gauge HBM 6/120 xy 11). The axial deformations as well as the lateral deformations in the middle part of the specimen were measured with these strain gauges, and the volumetric variation in the pre-peak part was determined. A detail of the three smallest specimens with the glued strain-gauges is reported in Fig. 1.c

For the two remaining specimen sizes, $h$=100 (C4) and 190 mm (C5), a manual load controlled uniaxial compression machine with a capacity of 3000 kN was used. The choice of this kind of machine was chosen for the following reasons. First of all, the height of the specimens do not permit control of the post-peak $\sigma - \epsilon$ diagram under displacement control, due to the more brittle structural behavior. This aspect could be overpassed if the tests were controlled over a central part of the specimens, as performed by van Vliet and van Mier [19], or through lateral deformations [20]. The latter would have comported a very sophisticated test, which was not the author's intention. Secondly, the control of the explosive behavior of the specimens and the determination of the fragment sizes pushed the author toward the aforementioned solution. For these two larger sizes, loading cycles around the peak-load (characterized by a decrease of the slope in the load versus displacement diagram) were performed in order to capture the post-peak branch and to plot the entire curve. Unfortunately, as should have been easy to predict, only for one specimen (C44) it was possible to capture the softening part. On the other hand, two specimens (C41 and C42) were tested in displacement control with a different closed loop servohydraulic machine with a capacity of 1000 kN. The stiffness of this machine was not enough and an explosive failure occurred.

*2.3   Boundary conditions*

In uniaxial compression tests it is well-known how the boundary conditions play an important role. When a concrete specimen is loaded between rigid loading platens (steel), the lateral deformation of concrete is confined to the specimen ends (Fig. 2.a), which are forced to have the same lateral deformation as the rigid platens. In this case, shear-stresses develop between specimen and loading platen, causing a three-dimensional state of stress at the specimen ends.

An opposite trend comes out when loading platens with a low stiffness and a high Poisson's ratio are used (rubber or brushes) (Fig. 2.b). The platens are subjected to large lateral deformations and outward-directed shear forces develop at the interfaces, producing local splitting cracks.

Kotsovos [21] performed experiments on cylinders with an aspect ratio of 2.5 and with different frictional systems. He observed the same pre-peak behavior (in dimensionless form) for the different choices of loading system, and post-peak dimensionless stress-displacement curves characterized by increasing slope with decreasing the coefficient of friction. In order to minimize the interface friction, van Mier [22] and Vonk [23] developed brush platens. Wittmann et al. [24] tested normal-strength concrete cylinders by attaching at the ends two high-strength concrete disks of the same diameter. This system was also adopted by Lee and Willam [25].

The system adopted in the present compression tests comes from the analysis of the RILEM Technical Committee 148 SSC results [2]. The loading platens, they found, not only affect the post-peak behavior, but also the peak stress. Van Vliet and van Mier [13] observed an increase in peak stress by decreasing the slenderness (up to 200%), when the specimens were loaded between rigid steel platens, whereas an almost constant peak stress with the application of teflon interlayers. The softening branch, with both the systems, becomes steeper with increasing specimen height. These results suggested the use of two teflon layers of 150 $\mu$m thickness with oil in between and a specimen slenderness equal to one.

## 3    EXPERIMENTAL OBSERVATIONS

Only one representative curve for each of the five sizes has been selected, for graphical reasons. The summary of the experimental results for peak-load, stress at peak load and specific compressive energy is reported in Table 2. The experimental load vs. displacement diagrams for smaller specimens ($h$=10 (C1), 23 (C2) and 46 mm (C3)) are reported in Fig.3.a, while those related to the larger specimens ($h = 100$ (C4) and 190 mm (C5)) are reported in Fig.3.b. Moreover, a typical failure in the post-peak softening regime is shown in Fig. 4 (specimen C33).

### 3.1    Stress-deformation response

The nominal stress vs. nominal deformation curves are plotted in Fig. 5. These curves have been obtained from the load vs. displacement curves by dividing the load by the initial specimen cross-section and the displacement by the initial specimen heigth. The curves show an initial steadily increasing slope, due to the lower stiffness at the beginning of the test. This fact is due to the adjustment of the loading platens to the specimen surfaces and to the compressibility of the teflon interlayers. This transition can be appreciated from Fig. 6, in which the axial and lateral strains obtained from strain-gauges placed in the middle third of the specimen are plotted together with the axial strains obtained by dividing the piston-stroke by the specimen height. In the latter, the measured axial strains (called mean deformation, $\epsilon_m$, Fig. 6) also contain the deformation of the steel loading platens. This part is often substituted by a straight line with slope equal to the maximum pre-peak slope

7

of the force-displacement curve. In this paper, the experimental curves have been presented as they have been recorded without any correction. Another possible correction that could be done on the experimental curves is related to the different testing machine used for different specimen sizes. In this case, the two different experimentally evaluated stiffnesses for the set-ups, obtained with the teflon layers without any specimen, could be subtracted from the experimental diagrams.

After this initial part, the stress-strain path is nearly linear and this linear part is as more pronounced as the specimen is larger (Fig.5). The smaller the specimen, the more pronounced pre-peak nonlinearities are. After the peak stress, a gradual descending branch has been detected. To appreciate the shape of the stress-strain curve better, its normalized version obtained by dividing the stresses by the peak stress (Fig.7a) and the strains by the strain at the peak stress (Fig.7b) are reported. As can be deduced from Fig. 7, the stress-strain curve for different specimens are almost the same in the pre-peak regime, but, beyond the peak, the slope of the post-peak part decreases with decreasing specimen height. Van Mier [22] plotted the normalized stress versus post-peak displacement curves, in which the displacements are calculated as:

$$\delta = (\epsilon - \epsilon_{peak})h, \tag{1}$$

and obtained nearly overlapped curves. He concluded that, as the same displacement is needed to fracture the specimens, the post-peak deformation must be localized in a small zone, and cannot be interpreted as an average strain. This fracture localization of concrete uniaxial compression implies that strain cannot be used as state variable in constitutive laws. The dimensionless stress versus post-peak deformation diagrams for four cylindrical specimen sizes are plotted in Fig. 8. It can be effectively observed that these curves are close to each other, even if different initial slopes, indicating an increase in brittleness with size, is present.

## 3.2   Scatter in peak-stress

The values of the peak-stresses, which are commonly called *compressive strength*, are reported in Fig.9 by varying specimen sizes. It can be noticed how in compression a marked size effect does not come out and no relation with the specimen size is evident, as instead can be observed in tension [26–28] or in compression when localization is present [1]. The same results were obtained experimentally by the RILEM Committee 148 and numerically by Carpinteri et al. [29,30] by simulations with a boundary element approach. The scatter in the results is pronounced. What is interesting to observe is that the values even for the smallest size are comparable to the compressive strength of standard cubes. This permits us to affirm that, if friction is avoided or drastically reduced, the compressive strength of an existing concrete structure can be evaluated using very small drilling core specimens (Nondestructive Test Method).

8

The dissipated energy density can be evaluated by considering the area under the $P - \delta$ curve divided by the volume of the specimen. This is equivalent to considering the area under the stress-strain curve. For the smallest specimen size, the dissipated energy density has been evaluated by considering the area under the stress-strain curve up to the minimum value of the stress. The numerical values of these areas for each specimen are reported in Tab.2. The values are also plotted versus the characteristic specimen size in Fig. 15. This dissipated energy density undergoes severe scale effects, and the trend is a decrease by increasing the specimen dimension. This interesting result is discussed in the next section and a theoretical explanation is presented based on a fractal hypothesis for the fragment size distribution generated during the compression test.

# 4  FULL STRESS-STRAIN CURVES

In this section the full stress-strain curves for the smallest cylindrical specimens ($h$=10 mm) are presented and some considerations are proposed. An interesting discussion of full stress-strain curve is proposed in the paper by Armer and Grimer [31]. They considered the re-ascending stress-strain branch which is not usually considered. This phenomenon was also described by Nikitin [32] by using dynamic analysis.

The complete curve for specimen C13 is plotted in Fig. 10. After the specimen has been crushed down more or less to a heap of aggregates, the resistance to further deformation reaches a minimum for $\epsilon \simeq 0.5$, and then begins to increase once more to higher stresses. Armer and Grimer affirm the existence of a new higher peak, at which the aggregate itself begins to break down. From the present experimental tests (Figs.10 and 11) the author's opinion is that the re-ascending curve tends to an oblique asymptote rather than to a new peak. The increase of load will continue and when all the aggregates will be pulverized, the slope of the asymptote has to coincide with the test machine stiffness.

Physically, the valley zone BCD of the nominal stress versus average strain for the specimen C12 (Fig. 11) reflects the macroscale breakdown of the specimen and the following restructuring of the material into a new stable form.

The knowledge of the full load versus displacement (or nominal stress versus average strain) diagram can be very useful in a load-controlled experimental test. In this case, after the peak load (point B) a snap-through instability is evidenced, and a horizontal jump up to point D occurs. The energy under the curve BCD is released suddenly in a blasting way. Of course, point D corresponds to a new equilibrium configuration, which is usually not achievable, as the instantaneous release of energy is transformed into kinetic energy with expulsion of fragments. The curve, therefore,

can be used to determine the specific energy released in the case of load-controlled test.

In concrete diamond drilling it can be observed how the snap-trough phenomenon just described can be very useful to simulate numerically the necessary energy (elastic and kinetic) to break concrete and to determine the chip size. For crushing phenomena (in concrete recycling, for example) it is very interesting to observe that the energy required to fragment a specimen (or in general a concrete element) is much larger than the elastic energy or the energy under the softening curve. This is due to the fact that the fragmentation and the formation of smaller chips is related to the surface area of the chips and this strongly increases by decreasing the size of the chips.

Finally, the last part of the curve can be influenced by the confinement due to the interaction of the aggregates with the machine platens. The interaction can be compared with the confinement effect due to the steel reinforcement in building columns which undergo earthquakes. In this case, if the confinement is well designed, the evaluation of re-ascending curve for concrete can be very useful.

# 5    FRACTAL EXPLANATION OF SIZE EFFECTS ON DISSIPATED ENERGY DENSITY IN COMPRESSION

The performed compression tests have shown an evident decrease of dissipated energy density with increasing specimen dimension (Fig. 15). This interesting phenomenon can be interpreted by considering the fragmentation and the comminution theories. In this field, fractal geometry represents a very helpful tool to explain such a phenomenon [16,17]. Turcotte [18] in the formulation of his fragmentation theory explains the difficulties in developing comprehensive theories. A primary reason is that fragmentation involves initiation and propagation of fractures. Fracture propagation is a highly nonlinear process requiring complex models even for the simplest configuration. Fragmentation involves the interaction between fractures over a wide range of scales. If fragments are produced over a wide range of sizes and if natural scales are not associated with either the fragmented material, fractal distribution of fragment number versus size would seem to be expected [33].

Let us consider a concrete specimen which undergoes a compression test. As is shown in Fig.4, in the post-peak softening regime the specimen is characterized by the generation of a large number of fragments. After fragmentation, the number of fragments $N$ with a characteristic linear dimension greater than $r$ should satisfy the relation:

$$N = \frac{B}{r^D}, \tag{2}$$

where $B$ is a constant of proportionality, and $D$ is the fractal dimension.

In order to describe the mechanical meaning of the fractal exponent $D$, in Fig.12 some examples of discrete fragmentation model are presented, where fragmentation is a scale-invariant process that leads to a fractal distribution of chip sizes. Let consider a fractal cube and use it as the basis for a fragmentation model. The fragmentation is such that some blocks are retained at each scale but others are fragmented. In Fig.12.a two diagonally opposed blocks are retained at each scale. For this configuration we have $N_1 = 2$ for $r_1 = \frac{h}{3}$, $N_2 = 50$ for $r_2 = \frac{h}{9}$, and $N_3 = 1250$ for $r_1 = \frac{h}{27}$. In order to determine $D$, eq.(2) can be written as:

$$D = \frac{\log(N_{n+1}/N_n)}{\log(r_n/r_{n+1})}, \tag{3}$$

and then we can find for this case that $D = \log 25/\log 3 = 2.93$. This is the fractal distribution of a discrete set. The cumulative number of blocks larger than a specified size for the three highest orders are $N_{1c} = 2$ for $r_1 = \frac{h}{3}$, $N_{2c} = 52$ for $r_2 = \frac{h}{9}$ and $N_{3c} = 1302$ for $r_2 = \frac{h}{27}$, obtaining a value $D = 2.95$.

In Fig.12.b eight angular diagonally opposed blocks are retained at each scale. For this configuration we have $N_1 = 8$ for $r_1 = \frac{h}{3}$, $N_2 = 152$ for $r_2 = \frac{h}{9}$, and $N_3 = 2888$ for $r_1 = \frac{h}{27}$, so that $D = \log 19/\log 3 = 2.68$. The cumulative number of blocks larger than a specified size for the three highest orders are $N_{1c} = 8$ for $r_1 = \frac{h}{3}$, $N_{2c} = 160$ for $r_2 = \frac{h}{9}$ and $N_{3c} = 3048$ for $r_2 = \frac{h}{27}$, obtaining a value $D = 2.70$.

In Fig.12.c the limit case of localization is presented in which eighteen angular blocks are retained at each scale, while only nine central blocks are fragmented. For this configuration we have $N_1 = 18$ for $r_1 = \frac{h}{3}$, $N_2 = 162$ for $r_2 = \frac{h}{9}$, and $N_3 = 1458$ for $r_1 = \frac{h}{27}$, so that $D = \log 9/\log 3 = 2.00$. The cumulative number of blocks larger than a specified size for the three highest orders are $N_{1c} = 18$ for $r_1 = \frac{h}{3}$, $N_{2c} = 180$ for $r_2 = \frac{h}{9}$ and $N_{3c} = 1638$ for $r_2 = \frac{h}{27}$, obtaining a value $D = 2.05$.

The same value for $D$ can be obtained by retaining at each scale 18 blocks and fragmenting 9 blocks placed this time in the configuration displayed in Fig.12.d. In this case, $D = 2$, but differently from Fig.12.c when we obtained a surface in correspondence of the central part of the largest block, we observe that the fragmentation phenomenon is localized in different small zones. Localization does not mean in this case dissipation on a surface (fracture or shear band), but rather localization of failure in concentrated zones.

The fractal dimensions for the discrete set and for the cumulative statistics are nearly equal. In Fig.13 the cumulative statistics are reported for three fragmentation models.

The total volume (mass) of fragments is given by [33]:

$$V_f = \int\limits_{r_{min}}^{r_{max}} r^3 \mathrm{d}N, \tag{4}$$

11

since $r$ has been defined to be the cube root of the fragment volume. It is expected that there will be upper and lower limits to the validity of the fractal (power-law) relation for fragmentation. The upper limit $r_{max}$ is generally controlled by the size of the fragmented object ($r_{max} = k\sqrt[3]{V}$ [34]). The lower limit $r_{min}$ is likely to be controlled by the scale of the heterogeneities responsible for fragmentation (grain size). For a power-law (monofractal hypothesis) distribution of sizes, substituting $dN = -BDr^{(-D-1)}dr$, with $B$ a constant of integration, into eq.(4) and integrating gives:

$$V_f = \frac{-DB}{3-D} \left( r_{max}^{3-D} - r_{min}^{3-D} \right),$$ (5)

where, for $0 < D < 3$, the specification of $r_{min}$ is not necessary. In this case the volume (mass) of fragments is predominantly provided by the largest fragments, so that $V_f$ can be rewritten as:

$$V_f = \frac{-DB}{3-D} r_{max}^{3-D}, \quad \text{for} \quad 0 < D < 3,$$ (6)

and then

$$V_f = \frac{-DB}{3-D} k^{3-D} V^{1-\frac{D}{3}}.$$ (7)

On the other hand, the total surface area $A_f$ of the fragments is given by:

$$A_f = C \int_{r_{min}}^{r_{max}} r^2 dN,$$ (8)

where $C$ is a geometrical factor depending upon the average shape of the fragments. For a power-law distribution, substitution of $dN = -DBr^{-D-1}dr$ into eq.(8) and integrating gives:

$$A_f = \frac{-DBC}{D-2} \left( \frac{1}{r_{min}^{D-2}} - \frac{1}{r_{max}^{D-2}} \right).$$ (9)

If $0 < D < 2$, it is necessary to specify $r_{max}$ in order to obtain a finite total surface area for fragments. If $D > 2$, it is necessary to specify $r_{min}$ in order to constrain the total surface area to a finite value. Usually the surface area of the smallest fragments dominates:

$$A_f = \frac{-BDC}{D-2} \frac{1}{r_{min}^{D-2}}.$$ (10)

12

It can be assumed that the energy dissipated to produce a new free surface in the fragmentation process is provided by the product of specific energy absorbing capacity $\beta_F$ and the total surface area $A_f$, for $2 < D < 3$ [17]:

$$W = \beta_F A_f = \beta_F A_f \frac{V}{V} \tag{11}$$

in which $\beta_F$ should be have dimension of $[F][L]^{(D-1)}$. From eq.(7), $V$ can be expressed as:

$$V = V^{D/3} V_f \frac{3-D}{-DB} k^{D-3} = \frac{r_{max}^3}{k^3}. \tag{12}$$

In this case it is possible to have, from eq.(6) and eq.(7):

$$W = \beta_F A_f \frac{V}{V} = \beta_F A_f \frac{V_f V^{D/3} \frac{3-D}{-DB} k^{D-3}}{\frac{r_{max}^3}{k^3}} = \tag{13}$$

$$= \left( \beta_f \frac{-BCD}{D-2} r_{min}^{2-D} r_{max}^D k^D \right) V^{\frac{D}{3}} = \mathcal{G}_F^* V^{\frac{D}{3}}.$$

The two extreme cases contemplated by eq.(13) are $D=2$, surface theory [35,36], when the dissipation really occurs on a surface ($W \propto V^{\frac{2}{3}}$) and by $D=3$, volume theory [37], when the dissipation occurs in a volume ($W \propto V$). In this case $\mathcal{G}_F^*$ presents the following physical dimension:

$$[\mathcal{G}_F^*] = \left( \beta_f \frac{-BCD}{D-2} r_{min}^{2-D} r_{max}^D k^D \right) = [F][L]^{D-1}[L]^{2-D}[L]^{-D} = [F][L]^{1-D}. \tag{14}$$

For $D = 2 \rightarrow [\mathcal{G}_F^*] = [F][L]^{-1}$, which is the canonical dimension for fracture energy, while for $D = 3 \rightarrow [\mathcal{G}_F^*] = [F][L]^{-2}$, which is the physical dimension of stress. The experimental cases of fragmentation are usually intermediate ($D \cong 2.5$) [18], as well as the size distribution for concrete aggregates due to Fuller [38].

If we consider $V = h^3$, we can write the expression of the dissipated energy density, from eq.(13):

$$S = \frac{W}{V} = \mathcal{G}_F^* h^{D-3}. \tag{15}$$

The relationship of dissipated energy density related to different sizes can be posed in logarithmic form:

$$\log S = \log \mathcal{G}_F^* + (D-3) \log h. \tag{16}$$

13

Eq.(16) represents a straight line with slope $(D-3)$ in the $\log S$ versus $\log h$ plane (Fig. 14). If $D = 2$, the slope is $-1$, as well as $D = 3$ implies a vanishing slope.

The same results can be obtained in a different way, by considering a sequence of scales of observation [39]. Considering $W$ as the global dissipated energy measured by the experimental set-up, $\mathcal{G}$ as the elastic energy release rate or the specific energy necessary to generate the unit area of fracture, which is by hypothesis invariant with respect to the scale of observation, we have:

$$W = \mathcal{G}A, \tag{17}$$

and then:

$$\mathcal{G} = \frac{W}{A} = \frac{SV}{A} = \frac{Sh^3}{h^2} = Sh. \tag{18}$$

If we consider a sequence of scale of observation, we have:

$$\mathcal{G} = S_1 h_1 = \ldots = S_{n-1} h_{n-1} = S_n h_n = S_{n+1} h_{n+1} = \ldots = S_\infty h_\infty, \tag{19}$$

where the first scale of observation could be the macroscopic one, with $S_1 h_1 = Sh$, $h$ being the characteristic linear dimension of the specimen, and the asymptotic scale of observation could be the microscopic one, with $S_\infty h_\infty = \mathcal{G}_F^* h^*$, $h^*$ being the measure of the fractal set representing the fragmented configuration. It is important to underline that the measure $h^*$ assumes finite value only for one particular value of $d_\omega$ equal to the fractal dimension of the set (Hausdorff dimension). For any other values of $d$, $h^* = 0$ for $d < d_\omega$ and $h^* = +\infty$ for $d > d_\omega$. From the equality between the extreme members we can write:

$$S = \mathcal{G}_F^* \left( \frac{h^*}{h} \right), \tag{20}$$

or:

$$S = \mathcal{G}_F^* \left( \frac{h^{1-d_\omega}}{h} \right), \tag{21}$$

where $0 < d_\omega < 1$ is the decrement of the topological dimension due to fragmentation. Taking the logarithms of both members of eq.(21) we obtain:

$$\log S = \log \mathcal{G}_F^* - d_\omega \log h, \tag{22}$$

where $d_\omega = 3 - D$ can be considered as the decrement of the topological dimension of the set in which energy dissipation occurs. When $d_\omega = 1$ we obtain $D = 2$ (localization) ; when $d_\omega = 0$ we have $D = 3$ (volumetric dissipation). Localization

assumes here the meaning of dissipation localized in concentrated zones. Eq.(22) is identical to eq.(16).

The values of dissipated energy density for the three smallest sizes are plotted in Fig. 15.a against the specimen size in a bilogarithmic plane. The values for the four available sizes are instead reported in Fig.15.b. The size effect is represented by the slope of the linear regression of the points of the diagram. It is evident how the dissipated energy density decreases with increasing specimen size.

As may be seen from Fig.15, the slope of the dissipated energy density decrease proves to be equal to 0.67 when only three specimen sizes are considered, and to 0.97 when considering the fourth size. We have considered the two different cases as the fourth size has been tested with a different procedure which can cause variations in energy estimation. In the former case, the physical meaning reveals an energy dissipation on a fractal space of dimension 2.33, while in the latter case the dissipation occurs on a fractal space of dimension 2.03, i.e., very close to a 2-dimensional surface. In the second case, as the fractal space is close to a 2-dimensional surface, different interpretations, by using the classical euclidean geometry, could be also proposed. In this approach, however, the fractal approach has been chosen. It is therefore possible to obtain a constant (universal) dissipated energy density equal to 31 Nmm$^{-1.33}$ and to 74 Nmm$^{-1.03}$, respectively (Fig.16). The graphic interpretation of the renormalization procedure is given in Fig.14. The assumption of a fractal (or anomalous) physical dimension allows the determination of the dissipated energy density parameter $\mathcal{G}_F^*$, which results in independence of the scale. As it is easy to observe, in the latter case the renormalized dissipated energy density tends to be a fracture energy, the dissipation occurring on a fractal set very close to a 2-dimensional surface. Such a result confirms the localization of the dissipation on a surface [25]. The fractal nature of the fragments generated by the compressive test emerges very clearly at the size scale of the specimens. Momber [10] applied fragmentation theory to the study of compression and analyzed the fragments, determining a fractal exponent $D$ close to 2. On the other hand, the property of self-similarity is very likely to vanish or change at higher or lower scales, owing to the limited character of the particle size curve. The price to pay for obtaining a constant value is the loss of the classical physical dimensions for dissipated energy density. It is obviously very difficult to use these results in a structural analysis, a noneuclidean (or fractal) mechanics being not yet available, even if very important steps have been moved forward by Carpinteri et al. [40].

# 6 SCALE-INDEPENDENT CONSTITUTIVE LAW FOR CONCRETE IN COMPRESSION

The experimental curves $\sigma$ vs $\epsilon$, reported in Fig.5, show a marked scale dependence, in particular for what concerns the post-peak part. These curves $\sigma$ vs $\epsilon$, or $F$ vs. $\delta$, are in fact characterized by two different regimes. The first regime corresponds to the pre-peak elastic behavior, when microcracks form randomly in the specimen.

At this stage the external force linearly increases until it reaches the peak value and the statistical fluctuations are very small. In the second regime, which could be called "catastrophic", the interactions between the microcracks begin to rule the process, untill macrofractures form and propagate through the whole specimen. In large specimens this phenomenon could occur with a sudden release of stored elastic energy.

In this section, a renormalization procedure is proposed to obtain a unique constitutive relationship for softening in compression. By assuming damage occurring in a fractal sub-domain inside the specimen, energy dissipation becomes scale-dependent. Hence it should be substituted by a fractal quantity, which is the true material constant. The assumption that the energy dissipation occurs in a sub-domain characterized by a fractal dimension, imposes the definition of fractal strain (or dilatation).

Let us consider the external work $W$, which presents the physical dimension of $[F][L]$. The nominal dissipated energy density, $S = W/V$, is usually the dissipated energy over the specimen volume, so that it presents the physical dimension of $[F][L]^{-2}$ and can be evaluated by integration:

$$S = \frac{W}{V} = \int_{0}^{\epsilon_{max}} \sigma(\epsilon) \mathrm{d}\epsilon, \tag{23}$$

which represents the area under the $\sigma - \epsilon$ curve. Supposing that the energy dissipation does not occur in the specimen volume ($V \propto l^3$) but in a fractal domain of dimension $D$ ($V \propto l^D$), and considering $[\sigma] = [F][L]^{-2}$ as the nominal stress, in order to obtain a constant specific compression energy, the strain has to assume a physical dimension of $[L]^{-(D-3)} = [L]^{d_\omega}$ [40,41]. In fact, in this hypothesis, if $W$ is dissipated over a domain with physical dimension of $[L]^D$, we obtain:

$$[S] = \frac{[W]}{[V]} = \frac{[F][L]}{[L]^D} = [F][L]^{1-D}. \tag{24}$$

For $D=2$ (surface theory, dissipation occurring on a surface) $\rightarrow S = [F][L]^{-1}$, while for $D=3$ (volume theory, dissipation occurring on a volume) $\rightarrow S = [F][L]^{-2}$. Assuming to maintain the the nominal stress $\sigma$ with physical dimension of $[F][L]^{-2}$, from eq.23 we have:

$$[S] = [\sigma][\epsilon^*] = [F][L]^{-2}[L]^x = [F][L]^{1-D}, \tag{25}$$

and than:

$$x = 3 - D = d_\omega. \tag{26}$$

In the monofractal hypothesis, the renormalized strain therefore assumes the physical dimension of $[L]^{3-D}$, defined as the displacements $\delta$ divided by $l=[L]^{D-2}$.

By considering the fractal strain, a scale-invariant constitutive relationship can be obtained. In other words, the experimental diagrams related to the different sizes can be rescaled by considering the strain renormalization, and a clear superposition of the curves is evidenced. In Fig.17.a the strains are renormalized for $D$=2.67 as obtained from the fitting that considers only three sizes, while in Fig.17.b the dimension $D$=2.03 has been used. It is possible to observe how the curves tend to superpose one on each other and in particular how the variation in structural behaviour disappears.

Lastly, form Fig.17a, b, it can be observed how a renormalization (or a new definition) of the elastic modulus comes out. In fact, the elastic modulus is defined, from the classical Hooke Law's, as the ratio between the stress and the strain. In the present analysis we obtain:

$$[E^*] = \frac{[\sigma]}{[\epsilon^*]} = \frac{[F][L]^{-2}}{[L]^{-(D-3)}} = [F][L]^{D-5}, \tag{27}$$

and in the two limit cases for $D = 2$ (surface theory, dissipation occurring on a surface) $\rightarrow E$=[F][L]$^{-3}$, and assumes the physical dimension of a density, while for $D = 3$ (volume theory, dissipation occurring on a volume) $\rightarrow E$=[F][L]$^{-2}$ and we obtain the classical elastic modulus.

The renormalization previously presented is in good agreement with the methodology proposed by van Mier [42] in order to obtain a unique empirical stress-displacement relationship and applied to the present experimental curves (Fig. 8). In fact, in our results (Fig. 17) the renormalization strain has a physical dimension equal to 0.97, very close to 1, and then very close to a displacement. What is important to emphasize at this stage is that in compression we have dissipation of the energy over an area at small scales, while at large scales the energy dissipation occurs in a volume. This appears very interesting as it is the opposite trend with respect to tension, in which localization is evident for large specimens and not at small scales. Eventually, the renormalization procedure for large specimens ($D$=3) tends again to a stress-strain diagram, as $\epsilon^* = \epsilon$

# 7 CONCLUSIONS

Uniaxial compression tests were performed under displacement control on drilled cylindrical specimens obtained from a single concrete block over a very large scale range (1:19), the largest range available in the literature. The friction between specimen ends and testing machine platens was reduced by using two layers of teflon with oil in between. The experimental results show how, reducing the friction at the ends, the nominal compressive strength is not clearly affected by scale effects as is evident in tension. The tests performed on very small specimen sizes (10 mm diameter) and the independence of the dimension for the compressive strength allows us deep considerations for evaluating the effective strength of real concrete

structures, that undergo deterioration of the mechanical properties and represent a dramatic problem in Civil Engineering. The results can be considered as a staring point in order to reconsider the standard dimension for evaluating the compressive strength of high-strength concretes, using the same testing machines available in the laboratories.

In addition, the full stress-strain curve in compression has been determined, and from those results it can be evidenced a snap-through instability allowing to quantify the energy required for fragmentation. The determination of the full curve is also important in concrete recycling industry to quantify the energy necessary for destroying concrete structures, even in blasting.

Finally, a theoretical explanation for the size effect on the dissipated energy density has been proposed, from which it appears how the dissipation occurs in a fractal subspace of dimension comprised between a surface and a volume. A renormalization procedure for determining a constant dissipated energy density is also proposed and it comes out that, in the range of the tested specimens, the energy dissipation occurs in a fractal space very close to a 2-dimensional surface. This is in a good agreement with the hypothesis proposed by van Mier [22] and by Lee and Willam [25], which stated that energy dissipation in the post-peak regime is a localized surface-dominated fracture process, after the coalescence of microcracks in the peak regime. This hypothesis is however valid only when small specimen sizes are used, whereas for large specimen sizes a volumetric dissipation occurs, as proposed by Carpinteri and Ferro [43] in a forthcoming paper.

## 8   ACKNOWLEDGEMENTS

## References

[1]  A. Carpinteri, G. Ferro, I. Monetto, Scale effects in uniaxially compressed concrete specimens, Magazine of Concrete Research 51 (1999) 217–225.

[2]  R. of the Round Robin Test carried out by RILEM TC 148-SSC:, Strain-softening of concrete in uniaxial compression, Materials and Structures 30 (1997) 195–209.

[3]  H. Gonnermann, Effect of size and shape of test specimen on compressive strength of concrete, Proceedings ASTM 25 (1925) 237–250.

[4] R. Blanks, C. McNamara, Mass concrete tests in large cylinders, Journal of American Concrete Institute 31 (1935) 280–303.

[5] X. Jishan, H. Xixi, Size effect on the strength of a concrete member, Engineering Fracture Mechanics 35 (1990) 687–695.

[6] B. Barr, H. Abusiaf, S. Sener, Size effect and fracture energy studies using compact compression specimens, Mechanics of Materials 31 (1998) 36–41.

[7] Z. Bažant, Y. Kwon, Failure of slenedr and stocky reinforced concrete columns: tests of size effect, Materials and Structures 27 (1994) 79–90.

[8] G. Campione, S. Mindess, Size effect in compression of high strength fibre reinforced concrete cylinders subjected to concentric and eccentric loads, in: N. Banthia (Ed.), ACI Special Publication on Fibre Reinforced Concrete, 2001, pp. 86–91.

[9] A. Carpinteri, B. Chiaia, G. Ferro, Multifractal scaling law: an extensive application to nominal strength size effect of concrete structures, Tech. Rep. 51, Atti del Dipartimento di Ingegneria Strutturale del Politecnico di Torino (1995).

[10] A. Momber, The fragmentation of standard concrete cylinders under compression: the role of secondary fracture debris, Engineering Fracture Mechanics 67 (2000) 445–459.

[11] F. O. Slate, K. C. Hover, Microcracking in concrete, in: A. Carpinteri, R. Ingraffea (Eds.), Fracture Mechanics of Concrete, Martinus Nijhoff Publishers, The Hague, 1984, pp. 137–159.

[12] I. Vardoulakis, J. F. Labuz, E. Papamichos, J. Tronvoll, Continuum fracture mechanics of uniaxial compression on brittle materials, International Journal of Solids and Structures 35 (1998) 4313–4335.

[13] M. van Vliet, J. van Mier, Experimantal investigation of concrete fracture under uniaxial compression, Mechanics of Cohesive-Frictional Materials 1 (1996) 115–127.

[14] A. Carpinteri, N. Pugno, A fractal comminution approach to evaluate the drilling energy dissipation, International Journal for Numerical and Analytical Methods in Geomechanics 26 (2002) 499–513.

[15] A. Carpinteri, N. Pugno, One-, two- and three-dimensional universal laws for fragmentation due to impact and explosion, Journal of Applied Mechanics 69 (2002) 854–856.

[16] B. B. Mandelbrot, The fractal geometry of Nature, W.H. Freemann and Company,, New York, 1982.

[17] F. M. Borodich, Fractals and fractal scaling in fracture mechanics, International Journal of Fracture 95 (1999) 239–259.

[18] D. L. Turcotte, Fractals and fragmentation, Journal of Geophysics Research 91 (1986) 1921–1926.

[19] M. van Vliet, J. van Mier, Softening behaviour of concrete under uniaxial compression, in: F. Wittmann (Ed.), Fracture Mechanics of Concrete Structures, AEDIFICATIO Publishers, 1995, pp. 383–369.

[20] D. Jansen, S. Shah, Effect of length on compressive strain softening of concrete, Journal of Engineering Mechanics (ASCE) 123 (1997) 25–35.

[21] M. D. Kotsovos, Effect of testing techniques on the post-ultimae behavior of concrete in compression, Mechanics of Materials 16 (1989) 1–12.

[22] J. van Mier, Multiaxial strain-softening of concrete - part i: fracture and part ii: load-histories, Materials and Structures 19 (1986) 179–200.

[23] R. A. Vonk, Softening of concrete loaded in compression, Ph.D. thesis, Eindhoven University of Technology, The Netherlands (1992).

[24] F. Wittmann, V. Slowik, A. Alvaredo, Probabilistic aspects of fracture energy of concrete, Materials and Structures 27 (1994) 499–504.

[25] Y.-H. Lee, K. Willam, Mechanical properties of concrete in uniaxial compression, ACI Materials Journal 94 (1997) 457–471.

[26] G. Ferro, Effetti di scala sulla resistenza a trazione dei materiali, Ph.D. thesis, Politecnico di Torino (1994).

[27] A. Carpinteri, G. Ferro, Size effects on tensile fracture properties: a unified explanation based on disorder and fractality of concrete microstructure, Materials and Structures 27 (1994) 563–571.

[28] A. Carpinteri, G. Ferro, Scaling behaviour and dual renormalization of experimental tensile softening responses, Materials and Structures 31 (1998) 303–309.

[29] A. Carpinteri, F. Ciola, N. Pugno, Boundary element method for the strain-softening response of quasi-brittle materials in compression, Computers and Structures 51 (2001) 389–401.

[30] A. Carpinteri, F. Ciola, N. Pugno, M. G. G. Ferrara, Size-scale and slenderness influence on the compressive strain-softening behaviour of concrete, International Journal of Fracture and Fatigue of Engineering Materials and Structures 24 (2001) 441–450.

[31] G. Armer, F. Grimer, On the use of full stress-strain characteristics in structural analysis, Materials and Structures 22 (1989) 48–52.

[32] L. Nikitin, Failure of structures due to crack growth and damage, Structural Safety 12 (1993) 123–128.

[33] D. L. Turcotte, Fractals and chaos in geology and geophysics, Cambridge University Press, 1992.

[34] A. Carpinteri, Mechanical Damage and Crack Growth in Concrete: Plastic Collapse to Brittle Fracture, Martinus Nijhoff Publishers, Dordrecht, 1986.

[35] P. R. Rittinger, Lehrbuch der aufbereitungskunde, Berlin, 1937.

[36] F. Hönig, Grundgesetze der zerkleinerung, Tech. Rep. 378, VDI Forschungsheft (1936).

[37] F. Kick, Das gesetz der proportionalen widerstande, Leipzig, 1885.

[38] P. Stroeven, Fractals and fractography in concrete technology, in: Int. Symposium on Brittle matrix composities, Warsaw, Poland, 1991, pp. 1–10.

[39] R. Goldshtein, A. Mosolov, Fractal cracks, Journal of Applied Mathematics and Mechanics 56 (1992) 563–571.

[40] A. Carpinteri, P. Cornetti, A fractional calculus approach to the description of stress and strain localization in fractal media, Chaos, Solitons and Fractals 13 (2002) 85–94.

[41] A. Carpinteri, B. Chiaia, P. Cornetti, A scale-invariant cohesive crack model for quasi-brittle materials, Engineering Fracture Mechanics 69 (2002) 207–217.

[42] J. van Mier, Fracture Process of Concrete, CRC Press, Boca Raton, FL, 1996.

[43] A. Carpinteri, G. Ferro, Effects of specimen size on the dissipated energy density in compression, Mechanics of Materials, submitted.

| Specimen no. | Diameter (mm) | High (mm) | A (mm$^2$) | Weight g | Volume (mm$^3$) |
|---|---|---|---|---|---|
| C11 | 9.9 | 9.5 | 76.98 | 1.9 | 731.31 |
| C12 | 9.9 | 9.9 | 76.98 | 2.0 | 762.10 |
| C13 | 9.8 | 10.0 | 75.43 | 2.1 | 754.30 |
| C14 | 9.8 | 9.8 | 75.43 | 1.9 | 739.21 |
| C15 | 9.8 | 10.0 | 75.43 | 2.0 | 754.30 |
| C16 | 9.8 | 9.9 | 75.43 | 1.7 | 746.76 |
| C21 | 23.7 | 24.2 | 441.15 | 24.0 | 10676 |
| C22 | 23.7 | 24.2 | 441.15 | 24.0 | 10676 |
| C23 | 23.7 | 24.2 | 441.15 | 23.5 | 10676 |
| C24 | 23.7 | 24.6 | 441.15 | 24.3 | 10852 |
| C25 | 23.7 | 24.4 | 441.15 | 23.5 | 10764 |
| C26 | 23.7 | 23.9 | 441.15 | 23.9 | 10543 |
| C31 | 44.9 | 45.3 | 1583.4 | 160.0 | 71728 |
| C32 | 45.1 | 44.6 | 1597.5 | 160.0 | 71248 |
| C33 | 45.1 | 45.1 | 1597.5 | 161.0 | 72047 |
| C34 | 44.8 | 45.4 | 1576.3 | 159.0 | 71564 |
| C35 | 45.0 | 45.3 | 1590.4 | 161.0 | 72045 |
| C36 | 45.1 | 45.6 | 1597.5 | 161.5 | 72846 |
| C41 | 99.5 | 100.3 | 7775.6 | 1795 | 779893 |
| C42 | 99.6 | 100.2 | 7791.3 | 1770 | 780688 |
| C43 | 99.5 | 100.6 | 7775.6 | 1790 | 782225 |
| C44 | 99.5 | 100.5 | 7775.6 | 1805 | 781448 |
| C51 | 192.2 | 192.9 | 29013 | 12585 | 5596608 |
| C52 | 192.1 | 191.7 | 28983 | 12580 | 5556041 |
| C53 | 192.2 | 193.6 | 29013 | 12645 | 5616917 |
| C54 | 192.2 | 191.4 | 29013 | 12585 | 5553088 |

**Table 1.** Summary of geometrical characteristics of specimens.

| Specimen no. | Peak Load (daN) | Stress at Peak Load (N/mm²) | Stress-Strain Area (N/mm²) |
|---|---|---|---|
| C11 | 295 | 38.32 | 6.12 |
| C12 | 328 | 42.61 | 7.32 |
| C13 | 327 | 43.35 | 7.12 |
| C14 | 335 | 44.41 | 8.34 |
| C21 | 1289 | 29.22 | 2.51 |
| C22 | 1457 | 33.03 | 3.45 |
| C23 | 1229 | 27.86 | 2.75 |
| C24 | 1404 | 31.83 | 2.78 |
| C31 | 5298 | 33.46 | 1.33 |
| C32 | 6136 | 38.41 | 2.90 |
| C33 | 5813 | 36.39 | 2.62 |
| C34 | 6311 | 40.04 | 3.24 |
| C41 | 27247 | 35.04 | 0.32 |
| C42 | 39194 | 50.30 | 0.33 |
| C43 | 39231 | 50.45 | 0.20 |
| C44 | 29923 | 38.48 | 0.42 |
| C51 | 142400 | 49.08 | - |
| C53 | 132210 | 45.57 | 0.35 |

**Table 2.** Summary of experimental results for peak-load, stress at peak load and critical compressive energy density.

## List of Figures

Fig. 1. (a) Geometry of the five different concrete specimens; (b) overall view of the five specimen sizes; (c) particular of the three smallest specimens with the glued strain-gauges.
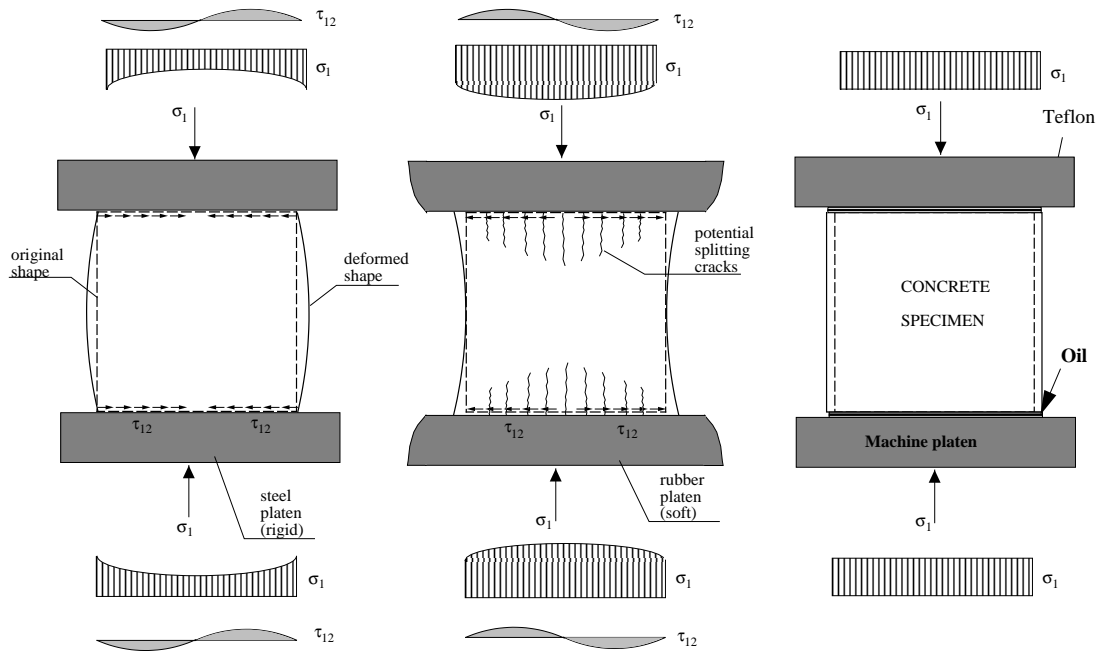
Fig. 2. Effect of loading platen response: (a) steel rigid platens; (b) soft platens and (c) adopted teflon layer proposed by van Vliet and van Mier (1995).
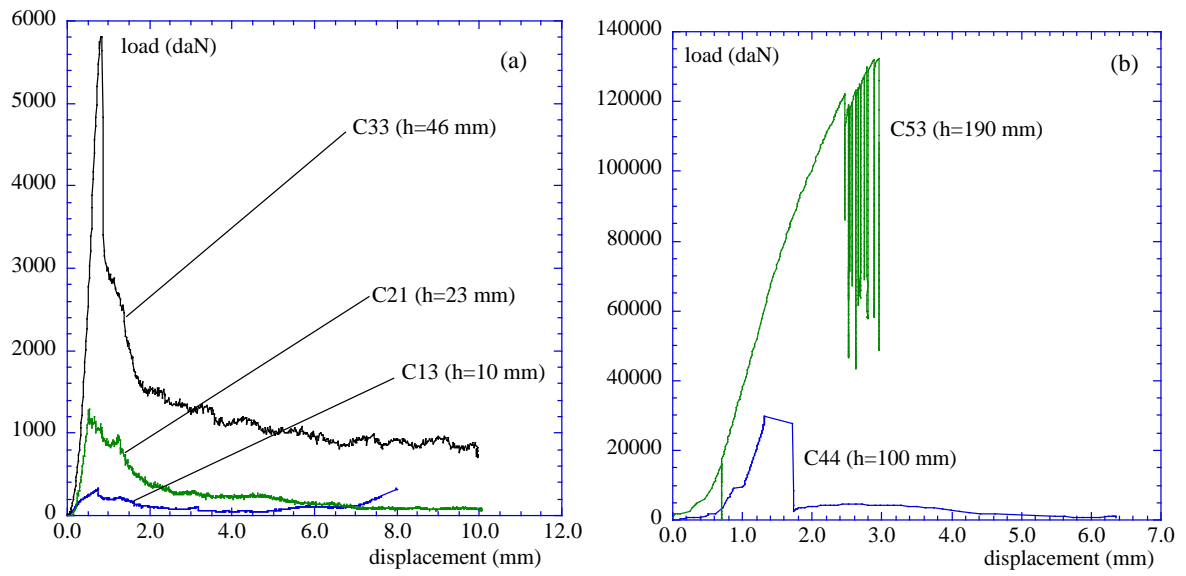
Fig. 3. Experimental load versus displacement curves: (a) small specimens, $h=10$ (C1), 23 (C2) and 46 mm (C3); (b) and large specimens, $h = 100$ (C4) and 190 mm (C5).
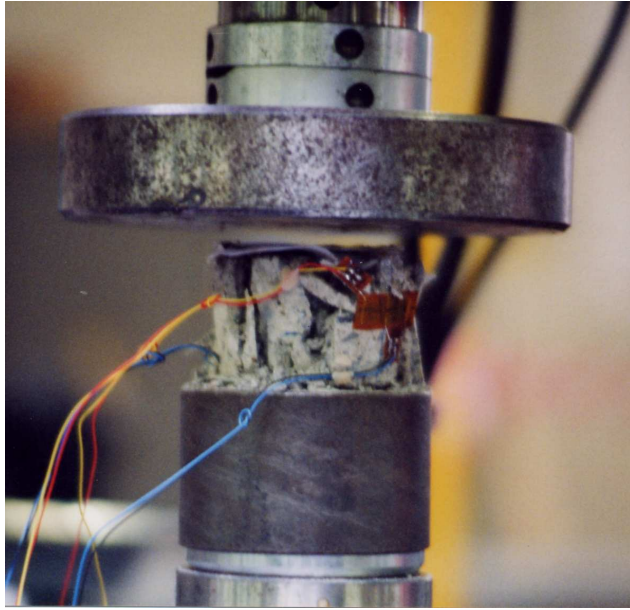
Fig. 4. Typical failure of a specimen in the post-peak softening regime.
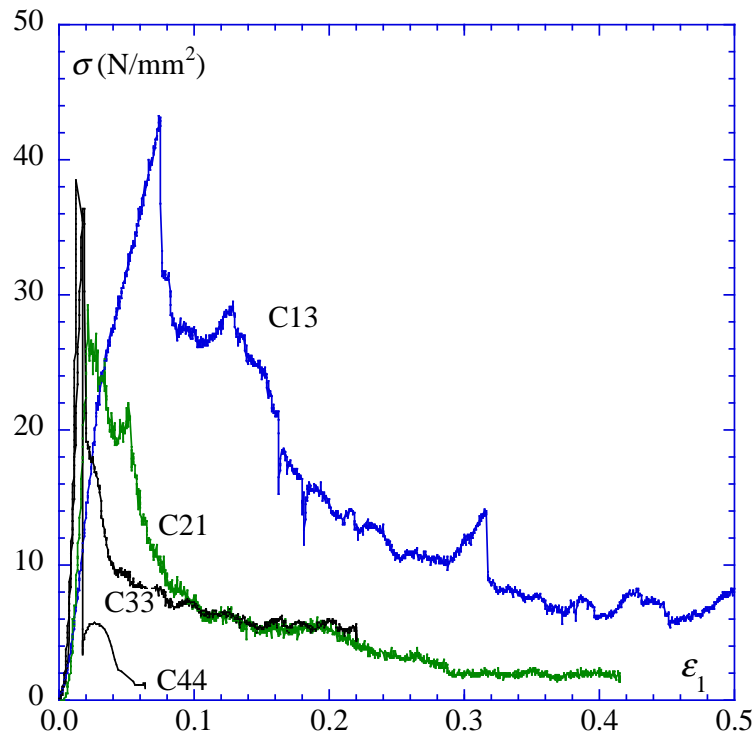
Fig. 5. Nominal stress vs. nominal strain diagrams for four different cylindrical specimen sizes.
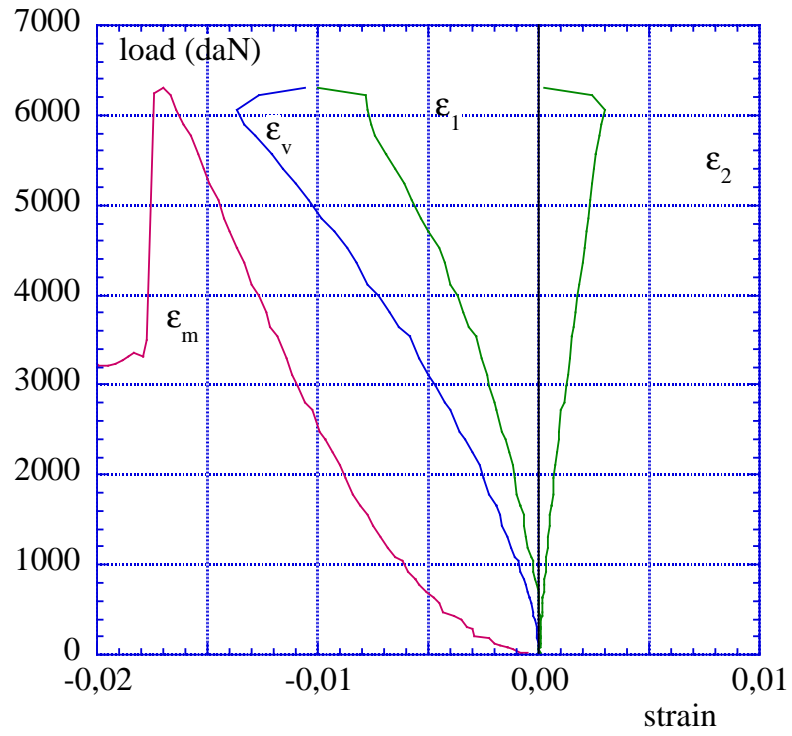
Fig. 6. Axial ($\epsilon_1$), lateral ($\epsilon_2$), volumetric ($\epsilon_v$) and mean ($\epsilon_m$) deformations for specimen C34.
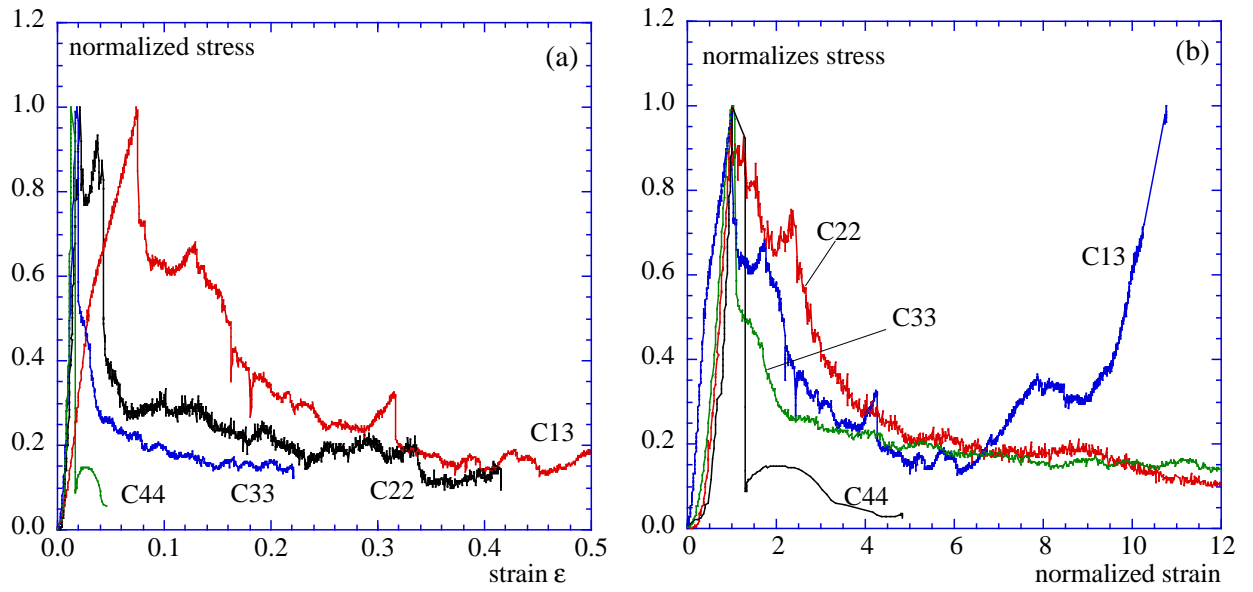
Fig. 7. (a) Normalized stress-strain diagrams for four different cylindrical specimen sizes; (b) normalized stress vs. normalized strain diagrams for four different cylindrical specimen sizes.
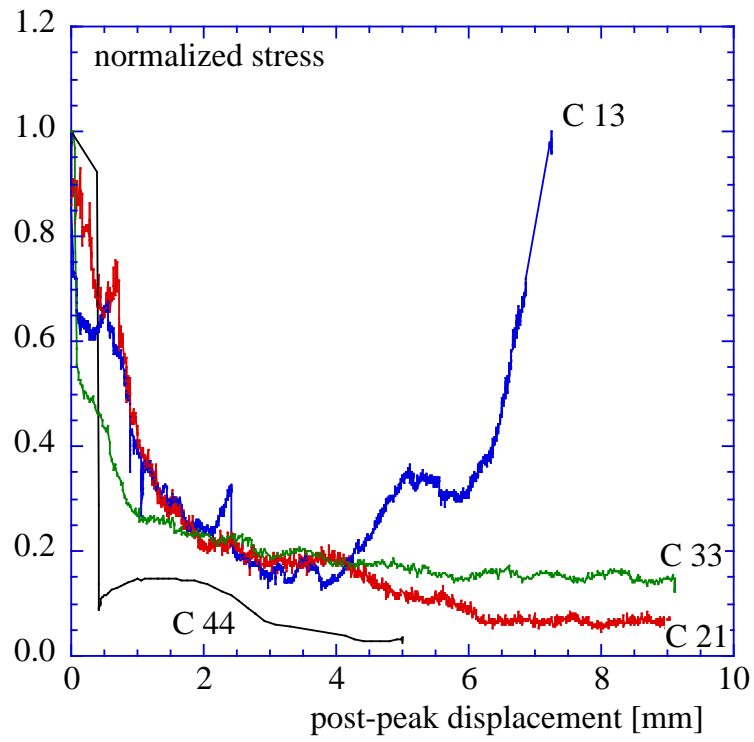
Fig. 8. Dimensionless stress versus post-peak displacement for four different cylindrical specimen sizes.
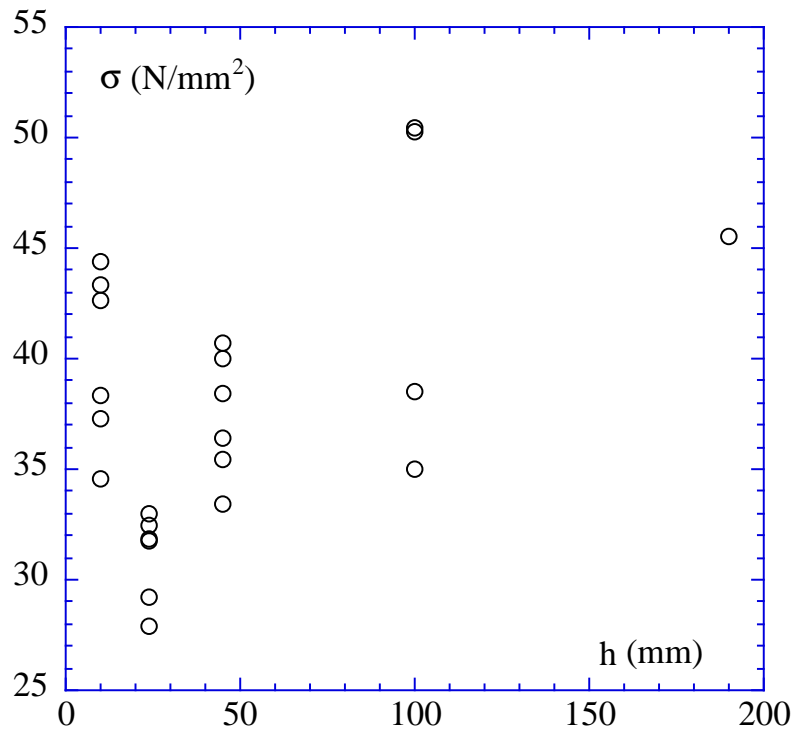
Fig. 9. Peak-stresses by varying specimen size.
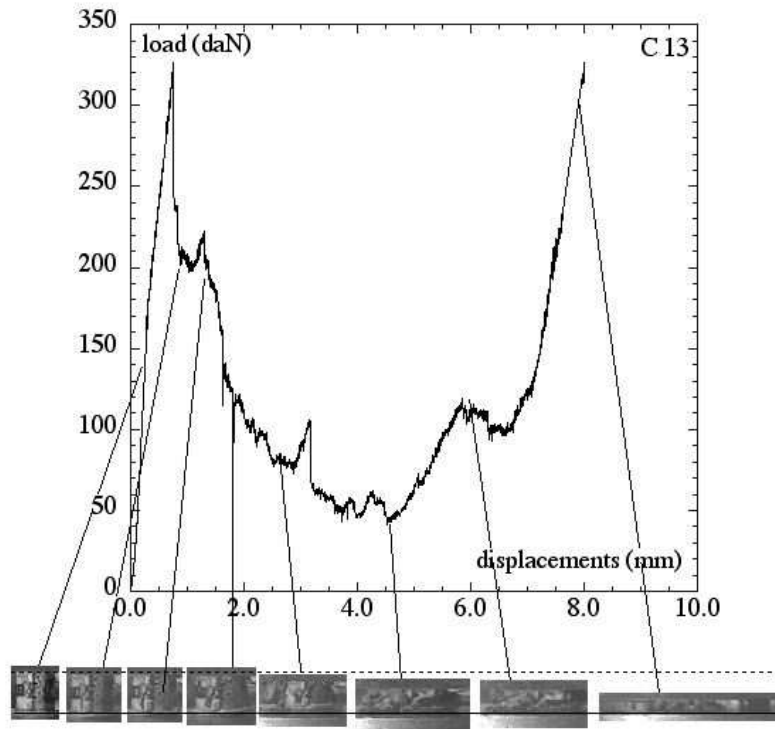
Fig. 10. Complete load versus displacement diagram up to compaction for the smallest specimen.
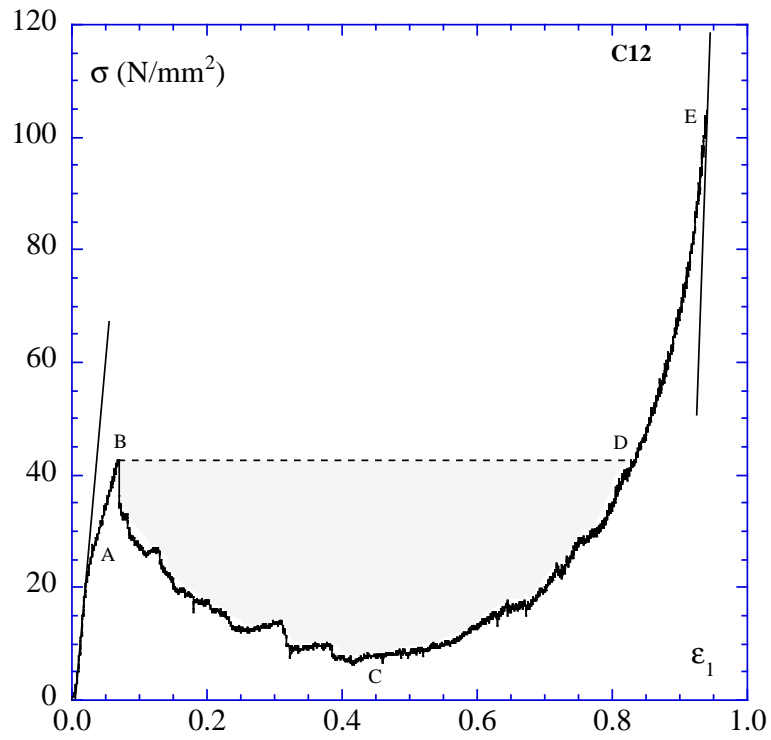
Fig. 11. Complete nominal stress versus nominal strain curve up to compaction for the smallest specimen size.
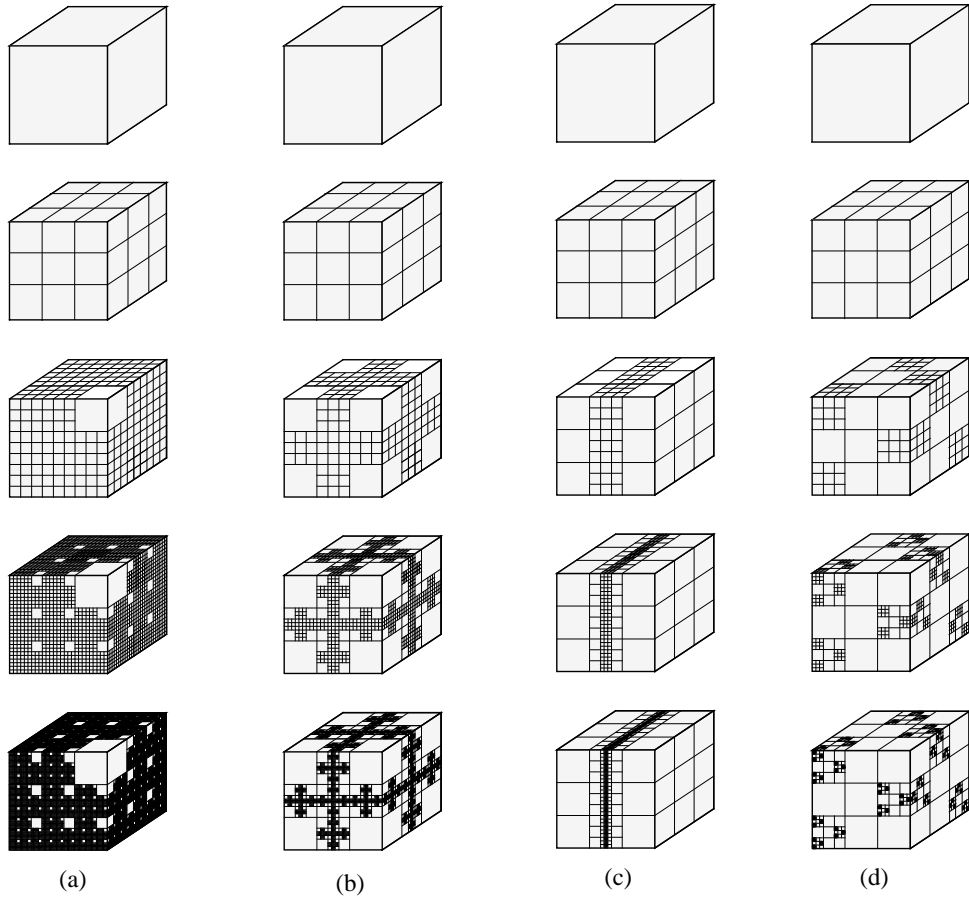
Fig. 12. Physical meaning of exponent $D$; (a) at each step only one cube is retained, while all the others are divided into 27 equal-sized cubes with $r_n=\frac{1}{3}r_{n-1}$ ($D$=2.93), very close to a volumetric fragmentation; (b) at each step the eight angular cubes are retained, while all the others 19 are divided into 27 equal-sized cubes with $r_n=\frac{1}{3}r_{n-1}$ ($D$=2.70);(c) and (d) at each step the nine central cubes are divided into 27 equal-sized cubes with $r_n=\frac{1}{3}r_{n-1}$, while the others 18 are retained ($D$=2.00), showing a localization of the dissipation energy.
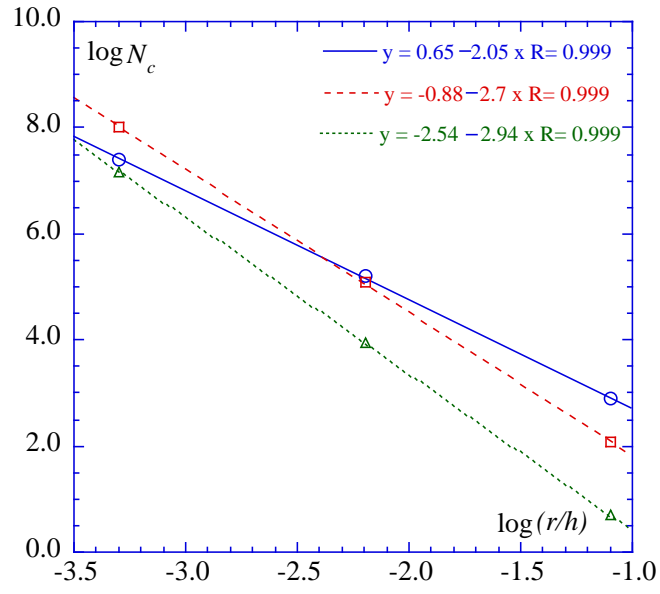
Fig. 13. Cumulative statistics for the fragmentation models proposed in Fig.12.
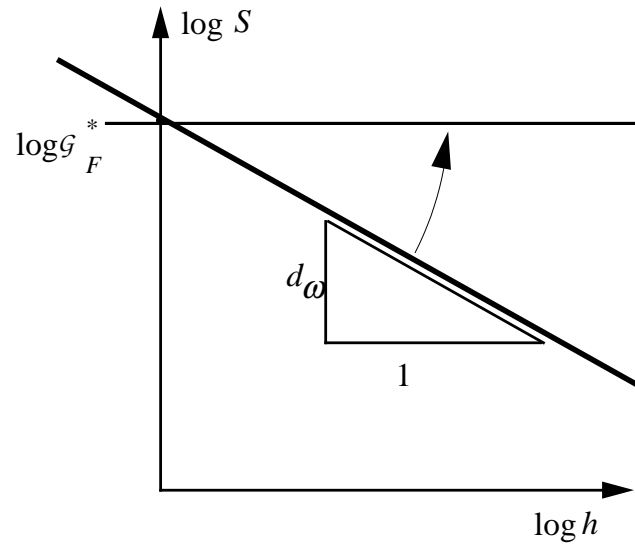
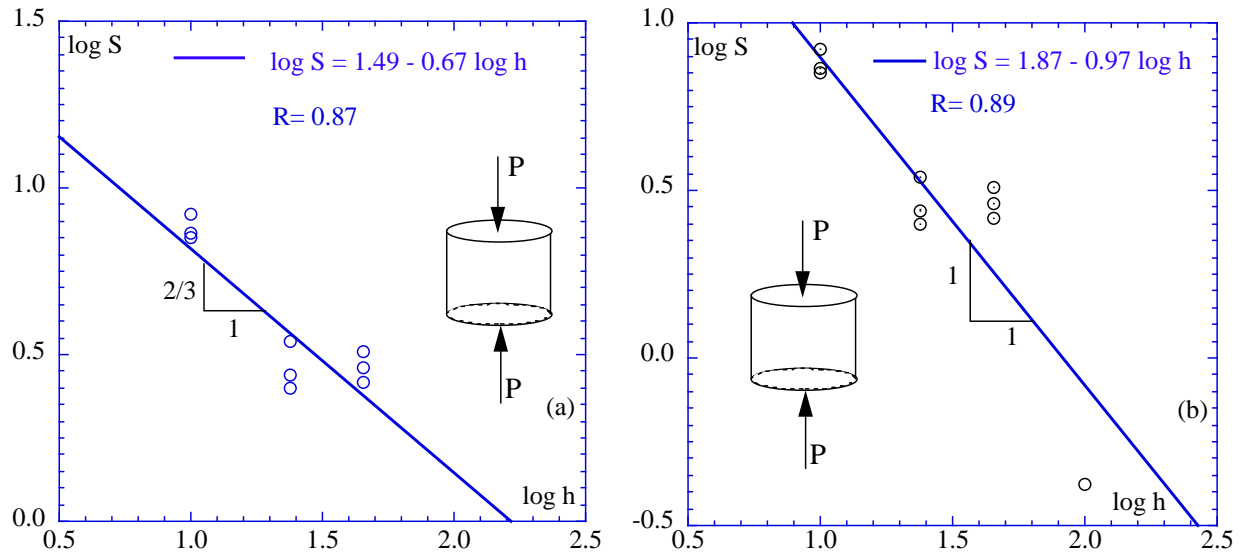Fig. 14. Size effect on dissipated energy density in compression.

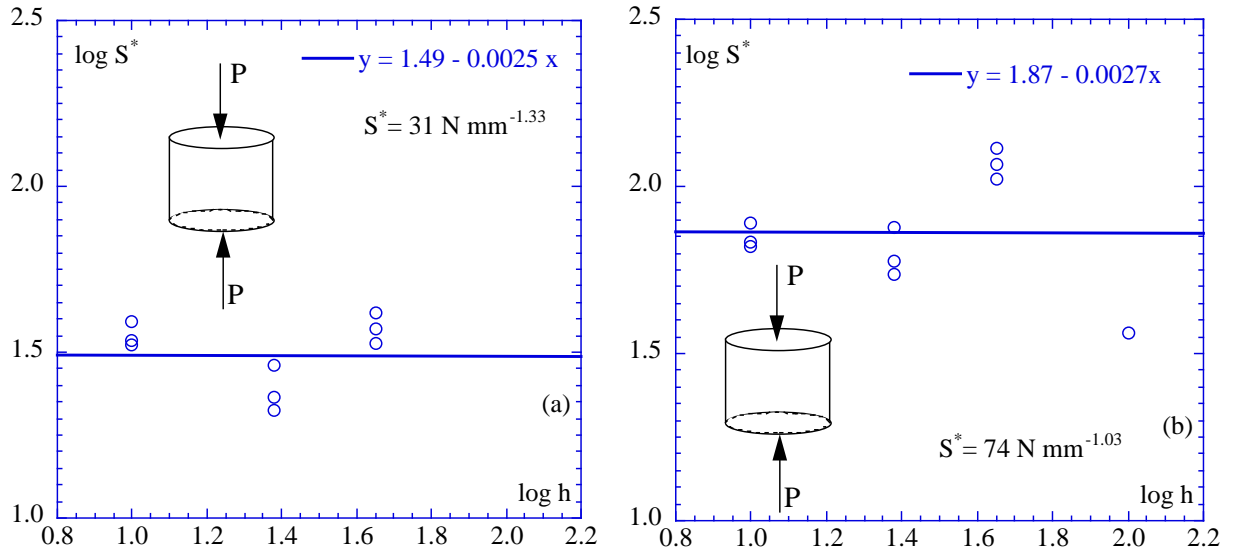Fig. 15. Size effect on dissipated energy density (experimental tests).

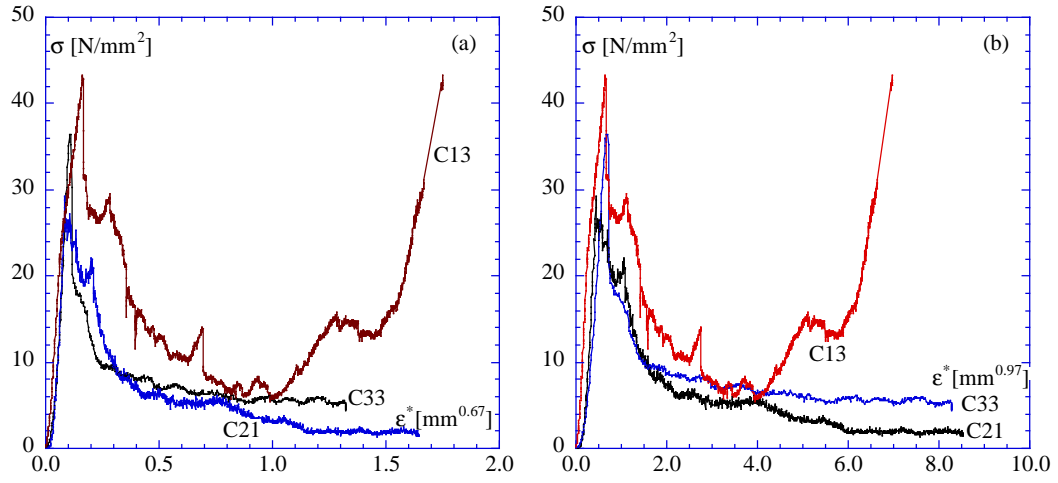Fig. 16. Renormalized value of dissipated energy density (experimental tests).

Fig. 17. Stress vs renormalized strain for three different specimen sizes: (a) $D$=2.33; (b) $D$=2.03.